

Evaluating the influence of soil plasticity on hydraulic conductivity based on a general capillary model

Zhixiong Zeng, Yu-Jun Cui, Jean Talandier

▶ **To cite this version:**

Zhixiong Zeng, Yu-Jun Cui, Jean Talandier. Evaluating the influence of soil plasticity on hydraulic conductivity based on a general capillary model. Engineering Geology, 2020, 278, pp.105826. 10.1016/j.enggeo.2020.105826 . hal-03045817

HAL Id: hal-03045817

https://enpc.hal.science/hal-03045817

Submitted on 17 Oct 2022

HAL is a multi-disciplinary open access archive for the deposit and dissemination of scientific research documents, whether they are published or not. The documents may come from teaching and research institutions in France or abroad, or from public or private research centers.

L'archive ouverte pluridisciplinaire **HAL**, est destinée au dépôt et à la diffusion de documents scientifiques de niveau recherche, publiés ou non, émanant des établissements d'enseignement et de recherche français ou étrangers, des laboratoires publics ou privés.



Distributed under a Creative Commons Attribution - NonCommercial| 4.0 International License

Version of Record: https://www.sciencedirect.com/science/article/pii/S0013795220317233
Manuscript_f2c2e2debab357962a835eb25da61821

Evaluating the influence of soil plasticity on hydraulic conductivity based on a general capillary model

Zhixiong Zeng[1*], Yu-Jun Cui[1], Jean Talandier[2]

1: Laboratoire Navier/CERMES, Ecole des Ponts ParisTech, 6 et 8 avenue Blaise Pascal, 77455 Marne La Vallée cedex 2, France
2: Andra, 1/7, rue Jean Monnet, 92298 Châtenay-Malabry cedex, France

***Corresponding author**

Zhixiong Zeng

Ecole des Ponts ParisTech
6–8 av. Blaise Pascal, Cité Descartes, Champs-sur-Marne
77455 Marne–la–Vallée cedex 2
France
Tel.: +33 781926608
Fax: +33 164153562
E-mail address: zhixiong.zeng@enpc.fr

© 2020 published by Elsevier. This manuscript is made available under the CC BY NC user license
https://creativecommons.org/licenses/by-nc/4.0/

Abstract: Soil hydraulic conductivity depends not only on the state variables such as void ratio and pore size distribution, but also on its physical/geotechnical properties. In this study, Atterberg limits, hydraulic conductivity and mercury intrusion porosimetry (MIP) tests were performed on MX80 bentonite/Callovo-Oxfordian (COx) claystone mixtures. Based on the experimental results obtained in this study together with the test data compiled from literature, a general capillary model considering N_p pores in series was used to evaluate the influence of soil plasticity on the relationship between hydraulic conductivity and pore size distribution. It was found that the best pore interconnection parameter N_p was highly dependent on the soil property. The larger the plasticity index, the larger the best N_p value and the more complex the pore interconnection. The relationship between the best N_p value and plasticity index could be well described by an exponential equation. The general capillary model was then improved to estimate the hydraulic conductivity of different soils. The estimated values using the improved general capillary model were finally compared with the measured ones and the good agreement between the measurement and estimation revealed the good performance of the proposed model.

Keywords: bentonite/claystone mixture; plasticity index; pore size distribution; hydraulic conductivity; general capillary model

1 Introduction

Water flow through soils is a matter of concern in many geotechnical, agricultural and environmental engineering practices, for instance, in the coupled consolidation analysis of clay foundation improvement and land reclamation with dredged clay (Yin 2009; Zeng et al. 2019a), in the design of isolating barriers in waste disposal facilities (Chapuis 1990) as well as in the assessment of water infiltration rate and percolation depth into agricultural land (Saffih-Hdadi et al. 2009). Obviously, this percolation process is dominated by the hydraulic conductivity of soils based on Darcy' law. It is therefore essential to quantitatively evaluate the hydraulic conductivity of soils for the geotechnical, agricultural and environmental issues.

In general, the hydraulic conductivity of saturated soils is experimentally measured using constant-head or fall-head methods (Deng et al. 2011). It can also be indirectly determined from the consolidation curve based on the Terzaghi's consolidation theory (Terzaghi 1943). It has been well documented that the hydraulic conductivity can be influenced by many factors, including the chemical properties of fluid, void ratio, mineralogy, grain size and shape, grain packing and orientation, pore size distribution and pore interconnection (Yin et al. 2009; Ren et al. 2016; Teng et al. 2019). Several investigators attempted to develop some empirical and theoretical models to predict the hydraulic conductivity from easily determinable physical characteristics of soils (Lapierre et al. 1990; Dolinar 2009). In most empirical models, the hydraulic conductivity was related to the selected properties of soils, such as void ratio (Berilgen et al. 2006; Dolinar 2009), effective grain size (Chapuis 2004) and representative pore size (Deng et al. 2015). However, the applicability of these empirical models to other soils needs further evaluation. Taking the channels of water flow through a cross section as uniform tubes, Kozeny (1927) proposed a theoretical model

known as Kozeny-Carman equation, which was further improved by Carman (1956):

$$k=C_{\mathrm{F}}\frac{1}{S_{\mathrm{s}}^2}\frac{\rho_{\mathrm{w}}g}{\mu\rho_{\mathrm{s}}^2}\frac{e^3}{1+e} \tag{1}$$

where k is the hydraulic conductivity; C_{F} is a dimensionless shape constant; S_{s} is the specific surface area; ρ_{w} and μ are the density and viscosity of water, respectively; g is the gravitational acceleration. Its performance was validated for sand (Ren et al. 2016). For clayey soils, which were generally characterized by an aggregated structure, pores could vary from very fine (intra-aggregate) to very coarse (inter-aggregate) (Kong et al. 2018). In that case, the pore size distribution became a crucial factor to be accounted for.

Based on the Poiseuille's equation for laminar flow through a cylindrical capillary, a capillary model was developed by Garcia-Bengochea et al. (1979) assuming parallel and cylindrical nonintersecting pores with different diameters:

$$k=\frac{\rho_{\mathrm{w}}gn}{32\mu}\sum_{i=1}^{m}d_{\mathrm{i}}^2 f(d_{\mathrm{i}}) \tag{2}$$

where n is the porosity of soil; m is the total number of pore intervals; i is the counter from 1 to m; d_i and $f(d_i)$ are the pore diameter and volumetric probability corresponding to i, respectively. In addition to the pore size distribution, the pore interconnection between soil sections could also influence the water flow. Childs and Collis-George (1950) and Marshall (1958) introduced a probabilistic approach to address this issue. Fig. 1a shows the water flow path through a capillary network in a soil fabric with two in-series sections having the same porosity n for a given length. The probability that a pore of diameter d_1 from one section joins a pore of diameter d_2 of another section is $[nf(d_1)][nf(d_2)]$. According to the basic idea of Poiseuille's equation, the smallest capillary between two capillaries in series governs the water flow through the capillaries (e.g. d_1

from a series of d_1 and d_2 in Fig. 1a) (Watabe et al. 2006). Correspondingly, Garcia-Bengochea et al. (1979) derived the following equation (known as the Marshall Model) for hydraulic conductivity:

$$k=\frac{\rho_w g n^2}{32\mu}\sum_{i_1=1}^{m}\sum_{i_2=1}^{m}\bar{d}^2 f(d_{i_1})f(d_{i_2}) \tag{3}$$

where i_1 and i_2 are the counters from 1 to m; d_{i_1} and d_{i_2} are the pore diameters corresponding to i_1 and i_2, respectively; $\bar{d}$ is the smaller one of d_{i_1} and d_{i_2}; $f(d_{i_1})$ and $f(d_{i_2})$ are the volumetric probabilities of occurrence of pores with diameters d_{i_1} and d_{i_2}, respectively. When a more complex soil fabric is considered, the water flow path through a capillary network in the soil fabric is schematically shown in Fig. 1b. The probability that a pore of diameter d_{i_1} from one section joins other pores of diameters $d_{i_2}, d_{i_3}, \cdots, d_{i_{N_p}}$ from other sections is $[nf(d_{i_1})][nf(d_{i_2})]\cdots\left[nf(d_{i_{N_p}})\right]$ (e.g. $[nf(d_1)][nf(d_2)][nf(d_3)][nf(d_4)][nf(d_5)][nf(d_6)]$ in Fig. 1b) and the diameter of the dominant flow channel $\bar{d}$ is the smallest one of $d_{i_1}, d_{i_2}, \cdots, d_{i_{N_p}}$ (e.g. d_6 from a series of d_1, d_2, d_3, d_4, d_5 and d_6 in Fig. 1b). N_p refers to the number of in-series pores in different sizes along a capillary water path for a given length. Under this circumstance, a general capillary model was proposed by Watabe et al. (2006; 2011):

$$k=\frac{\rho_w g n^{N_p}}{32\mu}\sum_{i_1=1}^{m}\sum_{i_2=1}^{m}\cdots\sum_{i_{N_p}=1}^{m}\bar{d}^2 f(d_{i_1})f(d_{i_2})\cdots f\left(d_{i_{N_p}}\right) \tag{4}$$

where $i_1, i_2, \cdots, i_{N_p}$ are the counters from 1 to m. The capillary and Marshall models correspond to Eq. (4) when N_p=1 and N_p=2, respectively. As a first attempt, Watabe et al. (2011) applied the general capillary model to the hydraulic conductivity prediction for glacial tills, sandy soils and clayey soils. They found that the N_p value which gives the best prediction was not the same for different soils. However, the influence mechanism of soil property on the hydraulic conductivity was not investigated in-depth.

In France, the clay-rich Callovo-Oxfordian (COx) sedimentary rock formation situated in the Meuse/Haute Marne site between 400 and 600 m depth was selected as the host rock to install the future repository for disposing radioactive wastes by the French National Agency for Nuclear Waste Management (ANDRA) (Andra 2005). The excavation of the underground tunnels for waste storage will produce a large amount of excess COx claystones to be dealt with. To reduce the financial costs and to better ensure the compatibility of chemistry with the host rock, the mixtures of the excavated COx claystone and MX80 bentonite were proposed to seal and backfill the underground drifts and shafts (Zeng et al. 2019b; 2020). After the installation in the repository, the selected mixtures are expected to exhibit permeability low enough to ensure the safety functions of the deep geological repository. Therefore, a comprehensive understanding of the permeability of bentonite/COx claystone mixtures with different bentonite fractions is essential to meet the performance target and to optimize the sealing/backfilling element design.

In this study, a series of Atterberg limits, constant-head hydraulic conductivity and mercury intrusion porosimetry (MIP) tests were carried out on MX80 bentonite and COx claystone mixtures. The plasticity index, hydraulic conductivity and pore size distribution of the mixtures with various bentonite fractions were determined. The general capillary model was applied to evaluate the hydraulic conductivities of bentonite/claystone mixtures together with those of other soils compiled from literature. The effect of plasticity index on the best N_p value was quantitatively determined, allowing an improved general capillary model to be proposed for the hydraulic conductivity estimation of different soils.

2 Materials and methods

2.1 Materials

125 The MX80 bentonite was taken from Wyoming in the USA, while the COx claystone was extracted
126 at a depth of around 490 m in the Underground Research Laboratory (URL) operated by ANDRA.
127 The bentonite and claystone were crushed to less than 2 mm. Their grain size distributions
128 determined by dry-sieving and hydrometer methods are shown in Fig. 2. The fractions of fine grains
129 (< 0.08 mm) determined by dry-sieving method are 19% and 0.3%, while the clay contents (< 2 μm)
130 determined by hydrometer method are 86% and 26%, for bentonite and claystone respectively.
131 Based on the X-ray diffraction analysis, the bentonite consists of montmorillonite (86%) and quartz
132 (7%), whereas the claystone comprises interstratified illite-smectite (40-45%), carbonates (30%) as
133 well as quartz and feldspar (25-30%).

134 Table 1 summarizes the chemical composition of the pore water extracted from the ANDRA
135 URL. To simulate the working environment of the bentonite/claystone mixtures, synthetic water
136 was used in the Atterberg limits and hydraulic conductivity tests. It was prepared by mixing the
137 components (Table 1) with deionized water until full dissolution.

138 *2.2 Determination of index properties*

139 Prior to the experiments, the bentonite and claystone, at their initial water contents of 11.4% and
140 6.1%, were first mixed together with different proportions of 10/90, 20/80, 30/70, 50/50 and 70/30
141 in dry mass. Subsequently, the specific gravity (G_s) values of bentonite, claystone and their
142 mixtures were measured using the pycnometer method in accordance with ASTM D854-10 (2010).
143 Referring to ASTM D4318-10 (2014), the liquid limit (w_L) and plastic limit (w_P) were determined
144 using percussion-cup and rolling test methods, respectively. Note that the bentonite, claystone and
145 their mixtures were wetted with synthetic water in the Atterberg limits test. For comparison, the
146 Atterberg limits of pure bentonite and claystone were also measured with de-ionized water.

147 *2.3 Hydraulic conductivity tests*

148 The hydraulic conductivity tests were performed on cylindrical samples of 50 mm diameter and 10
149 mm height. The pure claystone and mixtures were poured into a stainless steel ring and statically
150 compacted at a controlled displacement rate of 0.05 mm/min to various dry densities. Subsequently,
151 the compacted samples were transferred into the testing cell of 50 mm diameter and confined by a
152 cap which was blocked using a screw to prevent axial swelling deformation during hydration (Fig.
153 3). Afterwards, synthetic water was supplied from the bottom of the cell and the swelling pressure
154 during the hydration was monitored by the force transducer installed at the bottom of the cell. After
155 stabilization of the swelling pressure, the constant-head method was adopted to determine the
156 hydraulic conductivity of the compacted bentonite/claystone mixture in this study to gain good
157 accuracy (Pedescoll et al. 2012; Sandoval et al. 2017). The constant water pressure applied at the
158 bottom of samples was 10-200 kPa (about 1/10 of the stabilized swelling pressure), defining a
159 hydraulic gradient ranging from 100 to 2000. The evolution of injected water volume with time was
160 recorded. As the flow rate became steady, the tests were terminated and the corresponding hydraulic
161 conductivity k (m/s) was computed according to Darcy' law:

162 $$k=\frac{q}{iA} \tag{5}$$

163 where q is the steady flow rate (m^3/s); i is the hydraulic gradient; A is the cross-section area of
164 sample (m^2). All the tests were carried out at an ambient temperature of 20±1 °C.

165 *2.4 Mercury intrusion porosimetry tests*

166 After the hydraulic conductivity tests, the samples were extracted from the cell for the analysis of
167 pore size distribution by MIP. Freeze-drying method was applied for the sample preparation: the
168 saturated samples were carefully cut into small cubes with a side approximately equal to 1 cm; each

cube was rapidly immersed into liquid nitrogen previously vacuum-cooled below its freezing point (-196 °C) and then dehydrated in a vacuumed chamber for about 24 hours (Wang et al. 2014). After that, the samples were put into the low-pressure chamber of porosimeter with a working pressure from 3.6 to 200 kPa, prior to being transferred to the high-pressure chamber with a working pressure from 0.2 to 210 MPa (Bian et al. 2018). According to the Washburn equation, the pore entrance diameter d (μm) intruded by mercury at an applied pressure p (MPa) could be calculated, as follows:

$$d=\frac{4T_s\cos\alpha}{p} \tag{6}$$

where T_s is the interfacial tension (taken as 0.485 N/m); α is the contact angle between the mercury-air interface and soil (taken as 130°). The identified pore entrance diameter ranged from 350 to 0.006 μm.

3 Experimental results

3.1 Index properties

The index properties of the bentonite, claystone and their mixtures are shown in Table 2. As the bentonite fraction increased from 0 to 100%, the liquid limit determined with synthetic water increased from 41 to 291% while the plastic limit increased from 23 to 53%. The variation of the corresponding plasticity index with bentonite fraction is illustrated in Fig. 4. It clearly showed that the plasticity index determined with synthetic water increased from 17 to 238% with the increase of bentonite fraction from 0 to 100%. From Fig. 4, it could also be observed that the plasticity index of the mixtures lied below the dashed line, which could be expressed by the following equation:

$$I_{P\text{-}M}=I_{P\text{-}B}B/100+I_{P\text{-}C}(1\text{-}B/100) \tag{7}$$

where $I_{P\text{-}B}$ and $I_{P\text{-}C}$ and are the plasticity indices of bentonite and claystone, respectively; $I_{P\text{-}M}$ is the

191 mean weighted plasticity index of the bentonite and claystone in the mixture. This was consistent
192 with the observation of Pandian et al. (1995) on bentonite/clayey soil mixtures. It was suspected
193 that the mixing of two clays with various particle sizes and non-uniform clay plate sizes influenced
194 development of the diffuse double layer (Schanz et al. 2013) and a smaller thickness of diffuse
195 double layer surrounding the clay particles was expected in the bentonite/claystone mixture
196 (Sridharan et al. 1986). Accordingly, lower absorbed water on the external clay surface at the liquid
197 limit (Sridharan et al. 1986; Dolinar et al. 2007) and a lower plasticity index were observed
198 compared to the mean weighted value. With de-ionized water, the plasticity indices of bentonite and
199 claystone were found to be 488 and 17%, respectively. The plasticity index of bentonite with
200 synthetic water was significantly lower than that with de-ionized water. Yukselen-Aksoy et al.
201 (2008) found that the saline water could considerably reduce the plasticity index of soils with a
202 plastic index larger than 70%. This water chemistry effect could be explained by the diffuse double
203 layer theory. For the soils treated with saline water, the distance between two particles was
204 inversely with the square root of the salt concentration (Zhu et al., 2013). Thereby, a larger
205 inter-particle spacing and a larger amount of adsorbed water could be expected for the bentonite
206 with deionized water. As a result, a higher plastic index was observed compared to that with
207 synthetic water.

208 *3.2 Hydraulic conductivity*

209 The hydraulic conductivities of the samples with different bentonite fractions and void ratios are
210 summarized in Fig. 5. For comparison, the data of Karnland et al. (2008) on pure MX80 bentonite is
211 also presented. For the samples with 70% bentonite, it decreased from 1.00×10^{-12} to 9.91×10^{-14} m/s
212 as the void ratio decreased from 0.99 to 0.61; for the samples without bentonite, it decreased from

213 3.65×10^{-10} to 3.14×10^{-11} m/s as the dry density decreased from 0.50 to 0.36. Overall, there was a
214 linear relationship between hydraulic conductivity and void ratio. Similar phenomenon was
215 observed by Berilgen et al. (2006) and Dolinar (2009) when they studied the hydraulic conductivity
216 of crystallized kaolinite and Ca-montmorillonite. As the bentonite fraction decreased from 100% to
217 0%, the slope of the fitting lines (represented by the solid lines in Fig. 5) kept almost constant, with
218 a mean value of 6.577, while the intercept increased from $10^{-12.722}$ to $10^{-7.401}$. This phenomenon
219 indicated that the addition of claystone significantly reduced the sealing performance of the
220 mixture.

221 *3.3 Pore size distribution*

222 Fig. 6 presents the pore size distribution curves of samples with various bentonite fractions and void
223 ratios. On the whole, the cumulative curves of samples with larger void ratio lied above those of
224 samples with lower void ratio (Fig. 6a, c, e, g, i and k). Regarding the density function curves, the
225 samples with large bentonite fractions and low void ratios showed a typical bimodal pore size
226 distribution, with small pores at 0.25 μm and large pores at 10-22 μm. For the samples with low
227 bentonite fractions and large void ratios, another pore population at 0.17-0.52 μm (designated as
228 medium pores) could be observed apart from the small-pore and large-pore populations (Fig. 6b, d,
229 f, h, j and l). Following the definition of Bian et al. (2018) and Zeng et al. (2020), the pore sizes of 2
230 and 0.04 μm were adopted to delimit the large (2-350 μm), medium (0.04-2 μm) and small
231 (0.006-0.04 μm) pores. According to the accumulative curves, the corresponding void ratios of
232 large, medium and small pores were determined. Their variations with the total void ratio are
233 illustrated in Fig. 7. It appeared that the large-pore and medium-pore void ratios decreased while the
234 small-pore void ratio increased with the decrease of total void ratio. For the samples at the same

total void ratio, as the bentonite fraction increased, the large-pore and small-pore void ratios increased whereas the medium-pore void ratio decreased. Additionally, the void ratios for various populations became more uniform, showing a more complex pore size distribution. This phenomenon could be explained as follows: as a rule, the samples compacted at dry state were characterized by a bimodal porosity, with small and large pores (Wang et al. 2014; Bian et al. 2018). When the clay particles were saturated with water, the water molecules would be successively placed on the clay surface, increasing the inter-layer space (Wang et al. 2014; Bian et al. 2018). During this process, some initial small pores would become medium pores. Therefore, a decrease of the small-pore void ratio and an increase of the medium-pore void ratio could be expected after saturation. In the meanwhile, the placement of water molecules on the clay surface could also lead to clay particle exfoliation, clogging the large pores (Wang et al. 2014). Note that this process was strongly dependent on the dry density of soil. For the samples with low bentonite fraction, the void ratio of bentonite was relatively large and the placement of water molecules could be significant. Thereby, greater large-pore and medium-pore void ratios and smaller small-pore void ratio could be expected. On the contrary, with a high bentonite fraction, the void ratio of bentonite was relatively low; the limited void space did not allow full placement of water molecules, thereby limiting the microstructure change. For the samples with the same bentonite fraction, the decrease of total void ratio in the as-compacted state reduced the inter-aggregate pore volume (defined as the pores larger than 2 um by Wang et al. (2013)), but did not change the intra-aggregate pore volume. This explained why a greater large-pore (2-350 μm) void ratio was observed for the samples with a greater total void ratio after saturation, despite the much significant clogging process of large pores, thanks to the greater void ratio of bentonite.

4 Influence of plasticity index on hydraulic conductivity based on the general capillary model

From the general capillary model (Eq. (4)), the relationship between the hydraulic conductivity and the pore-size parameter (PSP) can be expressed by Eqs. (8) and (9) in the double-liner and double-logarithmic forms, respectively:

$$k=\frac{\rho g}{32\mu}\mathrm{PSP} \tag{8}$$

$$\log(k)=\log(\frac{\rho g}{32\mu})+\log(\mathrm{PSP}) \tag{9}$$

where PSP is calculated from the pore size distribution using Eq. (10):

$$\mathrm{PSP}=n^{N_\mathrm{p}}\sum_{i_1=1}^{m}\sum_{i_2=1}^{m}\cdots\sum_{i_{N_\mathrm{p}}=1}^{m}\bar{d}^2 f(\mathrm{d}_{i_1})f(d_{i_2})\cdots f\left(d_{i_{N_\mathrm{p}}}\right) \tag{10}$$

The parameter N_p refers to the pore interconnection and reflects the pore tortuosity. To further analyse the influence of N_p, Eq. (10) with N_p=1, 2, 3, 4, 5, 6, 7, 8, 9 and 10 was applied to compute the PSP of MX80 bentonite/COx claystone mixtures, Louiseville clay (Lapierre et al. 1990), Shanghai muddy clay (Tang and Yan 2015), Al-Ghat soil (Elkady et al. 2016), Wuhan clay (Zhao et al. 2016), Nanyang clay (Zhao et al. 2016), Maryland clay (Yuan et al. 2019) and Rajasthan monovalent bentonite (Jadda and Bag 2020) using the respective pore size distributions. As an example, the details of calculating the PSP value with N_p= 4 for the compacted MX80 bentonite/claystone mixture with a bentonite fraction of 30% and void ratio of 0.62 are described in Appendix A. In Fig. 8, the measured hydraulic conductivity is presented versus the PSP value for N_p=1, 2, 3, 4, 5, 6, 7, 8, 9 and 10, together with estimated hydraulic conductivity using Eq. (8). For clarity, all the data are presented in the double-logarithmic plane and the relationship between the estimated hydraulic conductivity and PSP value can be described by a straight line with a slope of 1. For comparison, also plotted in Fig. 8 is the relationship between the measured hydraulic conductivity and PSP determined by Watabe et al. (2006; 2011) for Québec glacial tills (N_p=1, 2

279 and 3), sandy soils (N_p=2, 3, 4 and 5) and clayey soils (N_p=2, 3, 4 and 5). For all the samples, the
280 larger the value of N_p, the lower the PSP value and the lower the estimated hydraulic conductivity
281 using Eq. (8), suggesting that the samples with a more complex pore interconnection had a lower
282 hydraulic conductivity. When the N_p value was lower than 4, the measured hydraulic conductivities
283 of the MX80 bentonite/COx claystone mixtures appeared on the right-hand of the estimated line. It
284 appeared that the theoretical estimations with N_p=5, 6, 6, 7, 9 and 10 were the best fit for the
285 hydraulic conductivities of MX80 bentonite/COx claystone mixtures with 0%, 10%, 20%, 30%, 50%
286 and 70% bentonite, respectively. This phenomenon indicated that the pore structure was more
287 complex for the samples with a higher bentonite fraction, which was consistent with the MIP results.
288 For the Louiseville clay, Québec glacial tills, sandy soils, clayey soils, Shanghai muddy clay,
289 Al-Ghat soil, Wuhan clay, Nanyang clay, Maryland clay and Rajasthan monovalent bentonite, the
290 theoretical equation showed the best performance for the hydraulic conductivity estimation when
291 the N_p was equal to 5, 3, 4, 5, 4, 5, 4, 6, 6 and 10, respectively.

292 As an easily determinable property, the plasticity index I_P represents the water quantity
293 adsorbed to the internal and external clay surfaces (Dolinar 2009). Generally, the higher the clay
294 fraction (< 2 μm), the larger the plasticity index (Seed 1964; Shi and Herle 2015). As illustrated in
295 Fig. 1, N_p represents the number of in-series pores in various diameters for a given length.
296 Obviously, the larger the clay fraction, the smaller the grain size, the more complex the pore
297 interconnection and the larger the N_p value. To quantitatively evaluate the influence of soil property
298 on the N_p value, the best N_p values are plotted versus the plasticity index in Fig. 9 for various soils.
299 Note that the plasticity indices of sandy and clayey soils reported by Watabe et al. (2011) ranged
300 from 0 to 15.3 and from 20.5 to 30.7, respectively. In Fig. 9, the mean plasticity indices of 7.6 and

301 25.4 were considered for the sandy and clayey soils, respectively. This relationship could be
302 expressed by the following exponential function, with a correlation coefficient of 0.940:

303 $$N_p=11.587-8.423\exp^{-0.0096I_p} \quad (11)$$

304 According to Eq. (11), the best N_p values of MX80 bentonite/COx claystone mixtures with 0%,
305 10%, 20%, 30%, 50% and 70% bentonite, Québec glacial tills, sandy soil, clayey soil, Louiseville
306 clay, Shanghai muddy clay, Al-Ghat soil, Wuhan clay, Nanyang clay, Maryland clay and Rajasthan
307 monovalent bentonite were found to be 4.50, 5.22, 6.18, 7.25, 8.55, 9.90, 5.75, 3.16, 3.76, 4.99,
308 4.65, 4.97, 4.63, 5.11, 6.16 and 10.20, respectively. Note that the value of N_p applied to Eq. (10)
309 must be a natural number. In this study, two limit values of hydraulic conductivity were first
310 determined using Eq. (8) and (10) with two adjacent natural numbers of the estimated N_p and then
311 the hydraulic conductivity of samples was estimated by a linear interpolation. The relationship
312 between the estimated and measured hydraulic conductivities for different soils is shown in Fig. 10.
313 The estimated hydraulic conductivities agreed well with the measured values, with errors in the
314 range from 1/5 to 5 times the measured values in most cases. This good agreement confirmed the
315 performance of the proposed method in the estimation of hydraulic conductivity.

316 **5 Conclusions**

317 In this study, the hydraulic conductivity of bentonite/claystone mixtures with different bentonite
318 fractions and void ratios were experimentally determined, together with the pore size distribution.
319 The experimental results obtained and the data compiled from literature were interpreted using the
320 general capillary model considering N_p pores in series, allowing the influence of plasticity index on
321 the relationship between the hydraulic conductivity and the pore size distribution to be investigated.
322 The following conclusions can be drawn.

(1) There was a liner relationship between the logarithms of hydraulic conductivity and void ratio. The slope of the fitting lines, kept almost constant for the samples with various bentonite fractions whereas the intercept increased with the decreasing bentonite fraction, suggesting that the addition of claystone reduced the sealing performance of the mixture.

(2) According to the microstructure investigation, the dry density of bentonite is lower for the samples with lower bentonite fractions and larger void ratios and therefore, a larger medium-pore (0.04-2 μm) volume but a lower small-pore (0.006-0.04 μm) volume was observed after saturation due to the more significant swelling of bentonite.

(3) Based on the general capillary model, it was found that the higher the plasticity index, the larger the best value of N_p, indicating a more complex pore interconnection for the soils with higher plasticity. The relationship between N_p and plasticity index could be described by an exponential equation. Based on this equation, an improved general capillary model was proposed. The results estimated using this model were then compared with the measured ones and the good agreement of hydraulic conductivity between the measurement and estimation revealed the performance of the proposed model.

Acknowledgments

The authors are grateful to Ecole des Ponts ParisTech, the China Scholarship Council (CSC) and the French National Agency for Nuclear Waste Management (ANDRA) for their financial supports.

Appendix A. The details of calculating the PSP value with N_p=4 for the bentonite/claystone mixture sample with a bentonite fraction is 30% and void ratio of 0.62

According to Eq. (10), the pores should be divided into discrete intervals before the calculation of PSP. Generally, the smaller the discretized intervals, the more precise the calculation of PSP. However, more discretized intervals will increase the computation time. After performing several trial computations, the pores were divided into 33 groups in this study, as shown in Fig. 1A. According to the cumulative pore volume curve of the bentonite/claystone mixture sample with a bentonite fraction of 30% and void ratio of 0.62, the volumetric probability ($f(d)$) of each group (corresponding to different average diameters of d) was calculated. The pore volumetric probability distribution of the sample is summarized in Fig. 1A. Afterwards, N_p=4, m=33, n=0.62/(1+0.62)=0.38 and the pore volumetric probability distribution were substituted into Eq. (10). Fig. 2A is a flowchart showing the process of calculating the PSP value with N_p=4. The corresponding PSP value of the sample was calculated to be 0.0225 μm^2.

References

Andra, 2005. Dossier 2005 Argile - Synthesis: Evaluation of the Feasibility of a Geological Repository in an Argillaceous Formation (Meuse/ Haute-Marne Site). French National Radioactive Waste Management Agency, Chatenay-Malabry CEDEX 241 pp. Accessed 22 November 2018.

ASTM D854-10, 2010. Standard test methods for specific gravity of soil solids by water pycnometer. Soil and Rock, West Conshohocken, Pennsylvania.

ASTM D4318-10, 2014. Standard Test Method for Liquid Limit, Plastic Limit, and Plasticity Index of Soils. Soil and Rock, West Conshohocken, Pennsylvania.

Berilgen, S.A., Berilgen, M.M., Ozaydin, I.K., 2006. Compression and permeability relationships in

high water content clays. Applied Clay Science, 31(3-4), 249-261.

Bian, X., Cui, Y.J., Li, X.Z., 2018. Voids effect on the swelling behaviour of compacted bentonite. Géotechnique, 69(7): 593-605.

Carman P.C., 1956. Flow of gases through porous media. Butterworths, London.

Chapuis, R.P., 1990. Sand–bentonite liners: predicting permeability from laboratory tests. Canadian Geotechnical Journal, 27(1), 47-57.

Chapuis, R.P., 2004. Predicting the saturated hydraulic conductivity of sand and gravel using effective diameter and void ratio. Canadian geotechnical journal, 41(5), 787-795.

Childs, E.C., Collis-George, N., 1950. The permeability of porous materials. Proceedings of the Royal Society of London. Series A. Mathematical and Physical Sciences, 201(1066), 392-405.

Deng, Y.F., Tang, A.M., Cui, Y.J., Li, X.L., 2011. Study on the hydraulic conductivity of Boom clay. Canadian Geotechnical Journal, 48(10), 1461-1470.

Deng, Y.F., Yue, X.B., Liu, S.Y., Chen, Y.G., Zhang, D.W., 2015. Hydraulic conductivity of cement-stabilized marine clay with metakaolin and its correlation with pore size distribution. Engineering geology, 193, 146-152.

Dolinar, B., Miŝiĉ, M., Trauner, L., 2007. Correlation between surface area and Atterberg limits of fine-grained soils. Clays and Clay Minerals, 55(5), 519-523.

Dolinar, B., 2009. Predicting the hydraulic conductivity of saturated clays using plasticity-value correlations. Applied clay science, 45(1-2), 90-94.

Elkady, T.Y., Shaker, A., Al-Shamrani, M., 2016. Hydraulic conductivity of compacted lime-treated expansive soils. In Geo-China 2016 (52-59).

Garcia-Bengochea, I., Altschaeffl, A.G., Lovell, C.W., 1979. Pore distribution and permeability of

389 silty clays. Journal of the Geotechnical Engineering Division, 105(7), 839-856.
390 Jadda, K., Bag, R., 2020. Variation of swelling pressure, consolidation characteristics and hydraulic
391 conductivity of two Indian bentonites due to electrolyte concentration. Engineering Geology,
392 doi: 10.1016/j.enggeo.2020.105637.
393 Karnland, O., Nilsson, U., Weber, H., Wersin, P., 2008. Sealing ability of Wyoming bentonite
394 pellets foreseen as buffer material–laboratory results. Phys. Chem. Earth Parts A/B/C, 33,
395 S472-S475.
396 Kong, L.W., Zeng, Z.X., Bai, W., Wang, M., 2018. Engineering geological properties of weathered
397 swelling mudstones and their effects on the landslides occurrence in the Yanji section of the
398 Jilin-Hunchun high-speed railway. Bulletin of Engineering Geology and the Environment,
399 77(4), 1491-1503.
400 Kozeny, J., 1927. Uber kapillare Leitung des Wassers im Boden. Sitzungsber. Akad. Wiss. Wien
401 136:271–306.
402 Lapierre, C., Leroueil, S., Locat, J., 1990. Mercury intrusion and permeability of Louiseville clay.
403 Canadian Geotechnical Journal, 27(6), 761-773.
404 Marshall, T.J., 1958. A relation between permeability and size distribution of pores. Journal of Soil
405 Science, 9(1), 1-8.
406 Pandian, N.S., Nagaraj, T.S., Raju, P.N., 1995. Permeability and compressibility behavior of
407 bentonite-sand/soil mixes. Geotechnical Testing Journal, 18(1), 86-93.
408 Pedescoll, A., Knowles, P.R., Davies, P., García, J., Puigagut, J., 2012. A comparison of in situ
409 constant and falling head permeameter tests to assess the distribution of clogging within
410 horizontal subsurface flow constructed wetlands. Water, Air, & Soil Pollution, 223(5),

411 2263-2275.
412 Ren, X., Zhao, Y., Deng, Q., Kang, J., Li, D., Wang, D., 2016. A relation of hydraulic
413 conductivity-void ratio for soils based on Kozeny-Carman equation. Engineering geology, 213,
414 89-97.
415 Saffih-Hdadi, K., Défossez, P., Richard, G., Cui, Y.J., Tang, A.M., Chaplain, V., 2009. A method
416 for predicting soil susceptibility to the compaction of surface layers as a function of water
417 content and bulk density. Soil and Tillage Research, 105(1), 96-103.
418 Sandoval, G.F., Galobardes, I., Teixeira, R.S., Toralles, B.M., 2017. Comparison between the
419 falling head and the constant head permeability tests to assess the permeability coefficient of
420 sustainable Pervious Concretes. Case studies in construction materials, 7, 317-328.
421 Schanz, T., Khan, M.I., Al-Badran, Y., 2013. An alternative approach for the use of DDL theory to
422 estimate the swelling pressure of bentonites. Applied Clay Science, 83, 383-390.
423 Seed, H.B., Woodward, R.J., Lundgren, R. (1964). Fundamental aspects of the Atterberg limits. J.
424 Soil Mech. Found. Div. ASCE 90(6), 75–105.
425 Shi, X.S., Herle, I., 2015. Compression and undrained shear strength of remoulded clay mixtures.
426 Géotechnique Letters, 5(2), 62-67.
427 Sridharan, A., Rao, S.M., Murthy, N.S., 1986. Liquid limit of montmorillonite soils. Geotechnical
428 Testing Journal, 9(3), 156-159.
429 Tang, Y.Q., Yan, J.J., 2015. Effect of freeze–thaw on hydraulic conductivity and microstructure of
430 soft soil in Shanghai area. Environmental earth sciences, 73(11), 7679-7690.
431 Teng, J., Kou, J., Zhang, S., Sheng, D., 2019. Evaluating the Influence of Specimen Preparation on
432 Saturated Hydraulic Conductivity Using Nuclear Magnetic Resonance Technology. Vadose

433 Zone Journal, doi: 10.2136/vzj2018.09.0179.
434 Terzaghi, K., 1943. Theoretical soil mechanics. New York: Wiley.
435 Lapierre, C., Leroueil, S., Locat, J., 1990. Mercury intrusion and permeability of Louiseville clay.
436 Canadian Geotechnical Journal, 27(6), 761-773.
437 Wang, Q., Tang, A.M., Cui, Y.J., Delage, P., Barnichon, J.D., Ye, W.M., 2013. The effects of
438 technological voids on the hydro-mechanical behaviour of compacted bentonite–sand mixture.
439 Soils and Foundations, 53(2), 232-245.
440 Wang, Q., Cui, Y.J., Tang, A.M., Li, X.L., Ye, W.M., 2014. Time-and density-dependent
441 microstructure features of compacted bentonite. Soils and Foundations, 54(4): 657-666.
442 Watabe, Y., LeBihan, J.P., Leroueil, S., 2006. Probabilistic modelling of saturated/unsaturated
443 hydraulic conductivity for compacted glacial tills. Géotechnique, 56(4), 273-284.
444 Watabe, Y., Yamada, K., Saitoh, K., 2011. Hydraulic conductivity and compressibility of mixtures
445 of Nagoya clay with sand or bentonite. Géotechnique, 61(3), 211-219.
446 Yin, J.H., 2009. Influence of relative compaction on the hydraulic conductivity of completely
447 decomposed granite in Hong Kong. Canadian geotechnical journal, 46(10), 1229-1235.
448 Yuan, S.Y., Liu, X.F., Buzzi, O., 2019. Effects of soil structure on the permeability of saturated
449 Maryland clay. Géotechnique, 69(1), 72-78.
450 Yukselen-Aksoy, Y., Kaya, A., Ören, A.H., 2008. Seawater effect on consistency limits and
451 compressibility characteristics of clays. Engineering Geology, 102(1-2), 54-61.
452 Zeng, L.L., Cai, Y.Q., Cui, Y.J., Hong, Z.S., 2019a. Hydraulic conductivity of reconstituted clays
453 based on intrinsic compression. Géotechnique, 1-8.
454 Zeng, Z.X., Cui, Y.J., Zhang, F., Conil, N., Talandier, J., 2019b. Investigation of swelling pressure

455 of bentonite/claystone mixture in the full range of bentonite fraction. Applied Clay Science.
456 doi: 10.1016/j.clay.2019.105137.
457 Zeng, Z.X., Cui, Y.J., Zhang, F., Conil, N., Talandier, J., 2020. Effect of technological voids on the
458 swelling behaviour of compacted bentonite/claystone mixture. Canadian Geotechnical Journal,
459 doi: 10.1139/cgj-2019-0339.
460 Zhao L.Y., Xue Q., Wan Y., Liu L., 2016. A comparative study of anti-seepage performance of
461 clays with high and low liquid limits under drying-wetting cycles. Rock and Soil Mechanics,
462 37(2), 446-452.
463 Zhu, C.M., Ye,W.M., Chen, Y.G., Chen, B., Cui, Y.J., 2013. Influence of salt solutions on the
464 swelling pressure and hydraulic conductivity of compacted GMZ01 bentonite. Eng. Geol. 166,
465 74–80.

List of Tables

Table 1 Chemical composition of the synthetic water
Table 2 Index properties of MX80 bentonite, COx claystone and their mixtures

List of Figures

Fig. 1 Typical water flow paths in soils consisting of (a) two sections and (b) six sections (modified after Watabe (2006)). Note: the grey areas represent the solid particle and the arrows indicate the water flow paths
Fig. 2 Grain size distributions of MX80 bentonite and crushed COx claystone
Fig. 3 Layout of the experimental setups for hydraulic conductivity tests
Fig. 4 Variation of plasticity index determined using synthetic water with bentonite fraction
Fig. 5 Relationship between hydraulic conductivity and void ratio
Fig. 6 Pore size distributions of samples: (a) cumulative curves of samples with 0% bentonite, (b) density function curves of samples with 0% bentonite, (c) cumulative curves of samples with 10% bentonite, (d) density function curves of samples with 10% bentonite, (e) cumulative curves of samples with 20% bentonite, (f) density function curves of samples with 20% bentonite, (g) cumulative curves of samples with 30% bentonite, (h) density function curves of samples with 30% bentonite, (i) cumulative curves of samples with 50% bentonite, (j) density function curves of samples with 50% bentonite, (k) cumulative curves of samples with 70% bentonite and (l) density function curves of samples with 70% bentonite
Fig. 7 Variations of (a) large-pore, (b) medium-pore and (c) small-pore void ratios with respect to total void ratio
Fig. 8 Relationship between hydraulic conductivity and PSP
Fig. 9 Variation of N_P with plasticity index I_p
Fig. 10 Comparison between measured and estimated hydraulic conductivities using Eqs. (8), (10) and (11)
Fig. A1 Pore volumetric probability versus pore diameter for the sample with a bentonite fraction of 30% and void ratio of 0.62. The number above each bar indicates the pore volumetric probability in percent
Fig. A2 The flow chart of calculating the PSP value using Eq. (10) with N_p=4

496 **Table 1** Chemical composition of the synthetic water

Component	NaCl	$NaHCO_3$	KCl	$CaSO_4 \cdot 2H_2O$	$MgSO_4 \cdot 7H_20$	$CaCl_2 \cdot 2H_2O$	Na_2SO_4
Content (g/L)	1.950	0.130	0.035	0.630	1.020	0.080	0.700

497

498 **Table 2** Index properties of MX80 bentonite, COx claystone and their mixtures

Soil property	Claystone	Bentonite/claystone mixtures with different bentonite fraction (B)					Bentonite
		B=10%	B=20%	B=30%	B=50%	B=70%	
Water content (%)	6.1	6.6	7.2	7.7	8.8	9.8	11.4
Specific gravity	2.70	2.71	2.71	2.72	2.73	2.74	2.76
Liquid limit (%)	40	54	73	98	140	208	291
Plastic limit (%)	23	25	27	29	34	41	53
Plasticity index (%)	17	29	46	69	106	167	238

499

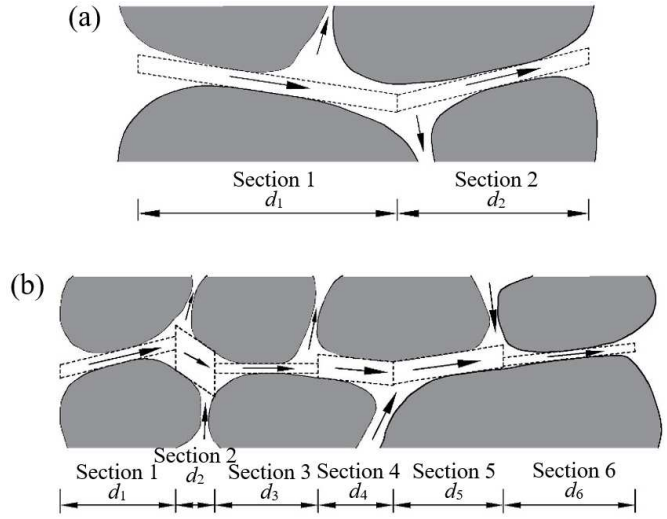
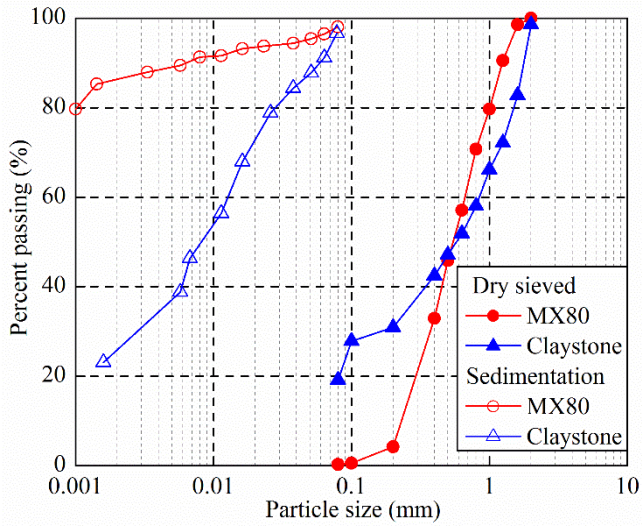
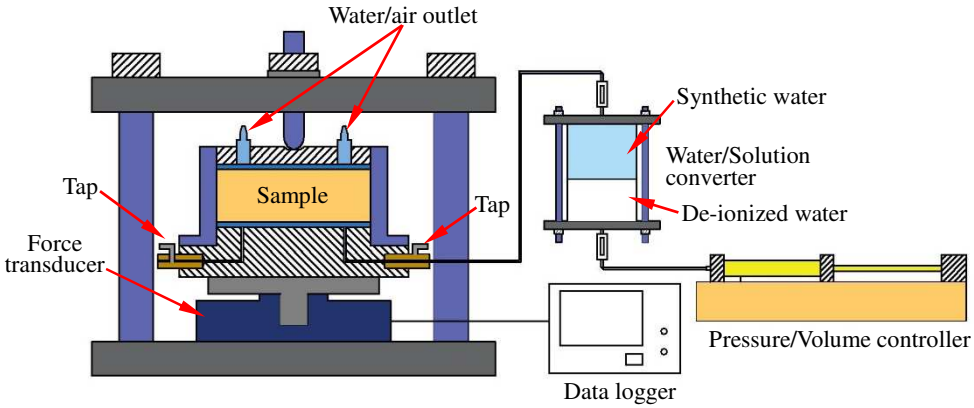


Fig. 1 Typical water flow paths in soils consisting of (a) two sections and (b) six sections (modified after Watabe (2006)). Note: the grey areas represent the solid particle and the arrows indicate the water flow paths

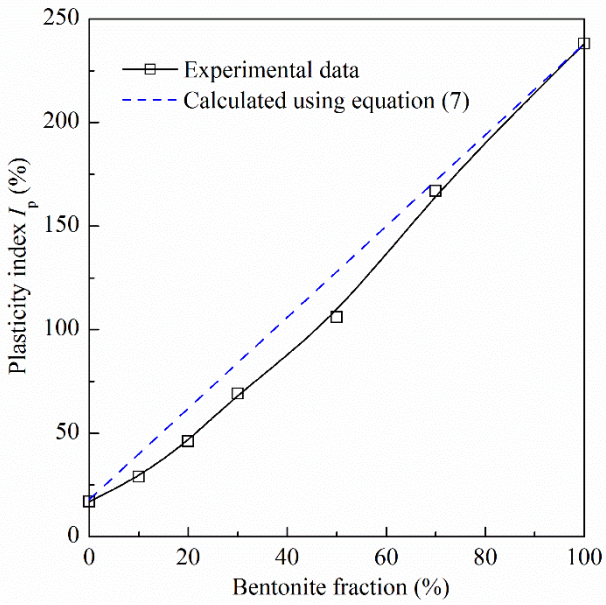


503
504 **Fig. 2** Grain size distributions of MX80 bentonite and crushed COx claystone



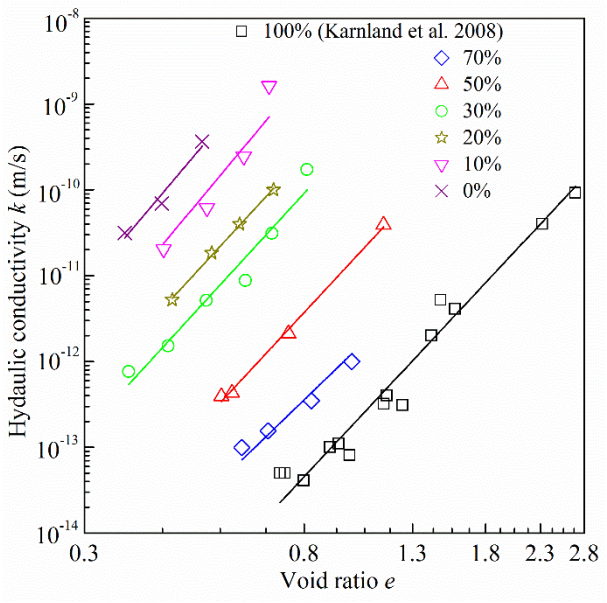
505

506 **Fig. 3** Layout of the experimental setups for hydraulic conductivity tests



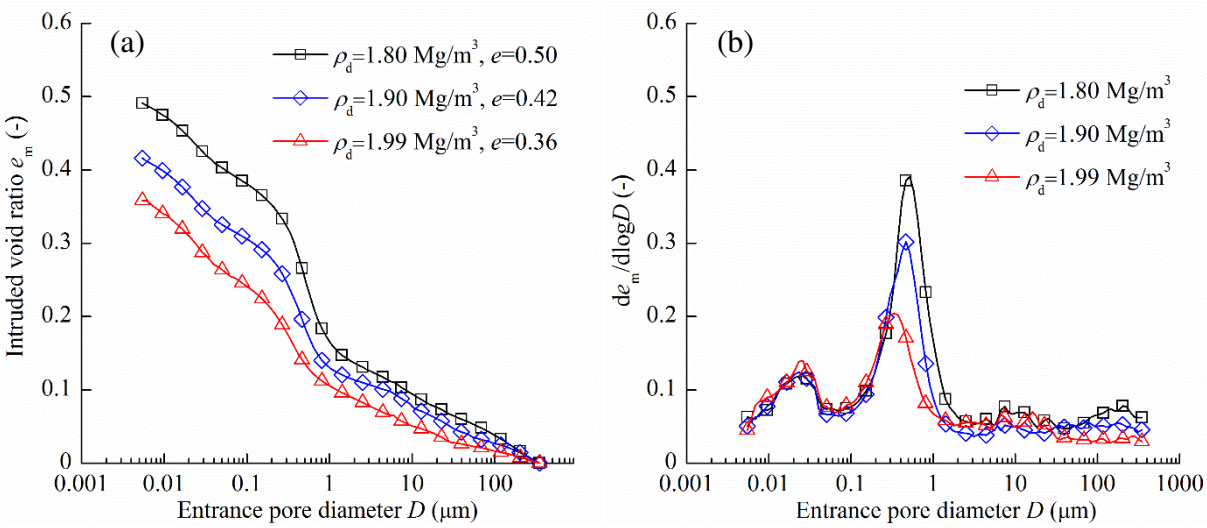
507

508 **Fig. 4** Variation of plasticity index determined using synthetic water with bentonite fraction

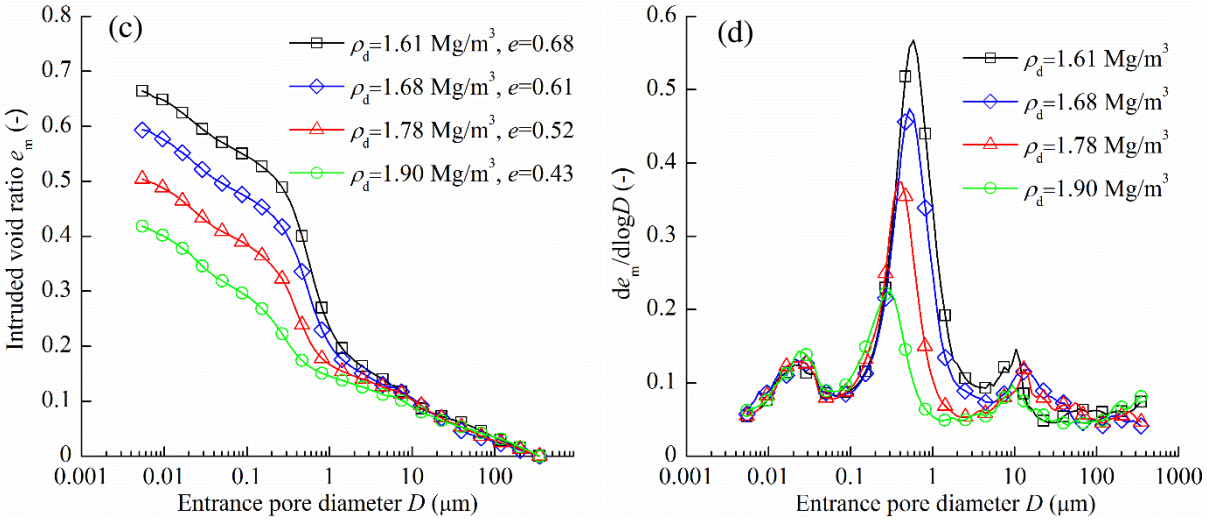


509

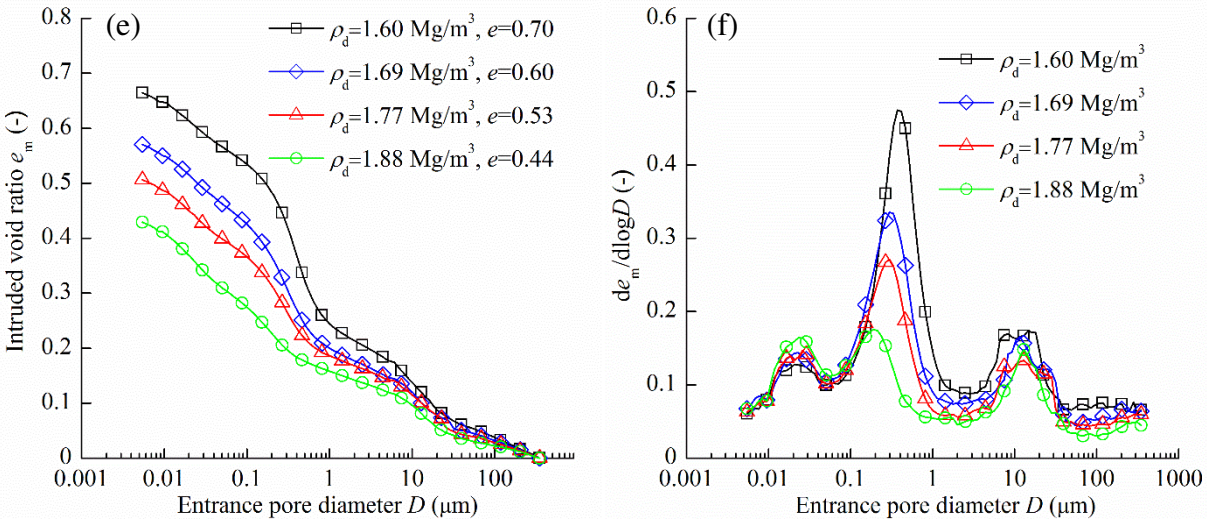
510 **Fig. 5** Relationship between hydraulic conductivity and void ratio


(a)
ρ_d=1.80 Mg/m^3, e=0.50
ρ_d=1.90 Mg/m^3, e=0.42
ρ_d=1.99 Mg/m^3, e=0.36
Intruded void ratio e_m (-)
Entrance pore diameter D (μm)
(b)
ρ_d=1.80 Mg/m^3
ρ_d=1.90 Mg/m^3
ρ_d=1.99 Mg/m^3
de_m/dlog$D$ (-)
Entrance pore diameter D (μm)

511


(c)
ρ_d=1.61 Mg/m^3, e=0.68
ρ_d=1.68 Mg/m^3, e=0.61
ρ_d=1.78 Mg/m^3, e=0.52
ρ_d=1.90 Mg/m^3, e=0.43
Intruded void ratio e_m (-)
Entrance pore diameter D (μm)
(d)
ρ_d=1.61 Mg/m^3
ρ_d=1.68 Mg/m^3
ρ_d=1.78 Mg/m^3
ρ_d=1.90 Mg/m^3
de_m/dlog$D$ (-)
Entrance pore diameter D (μm)

512


(e)
ρ_d=1.60 Mg/m^3, e=0.70
ρ_d=1.69 Mg/m^3, e=0.60
ρ_d=1.77 Mg/m^3, e=0.53
ρ_d=1.88 Mg/m^3, e=0.44
Intruded void ratio e_m (-)
Entrance pore diameter D (μm)
(f)
ρ_d=1.60 Mg/m^3
ρ_d=1.69 Mg/m^3
ρ_d=1.77 Mg/m^3
ρ_d=1.88 Mg/m^3
de_m/dlog$D$ (-)
Entrance pore diameter D (μm)

513

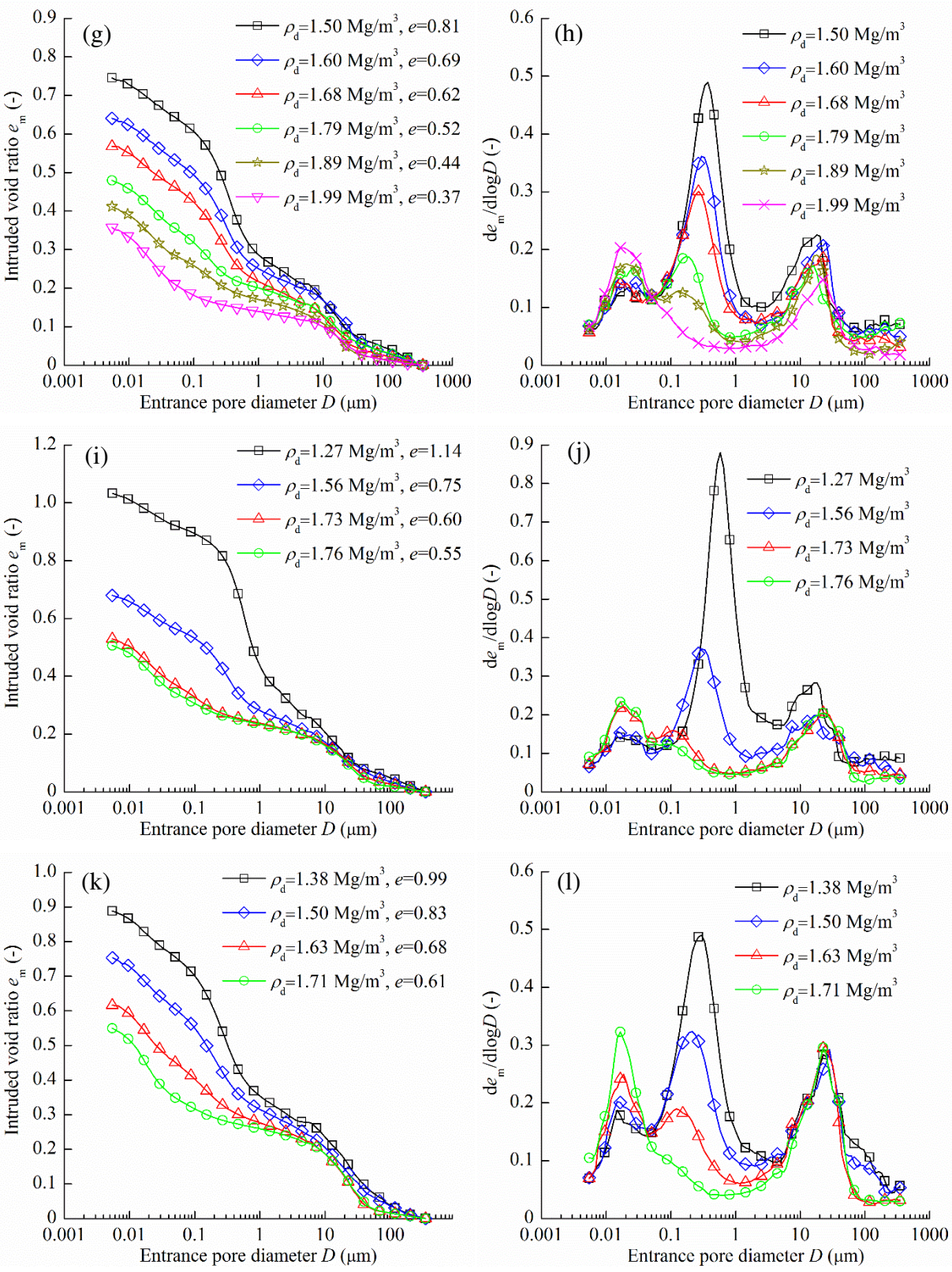


Fig. 6 Pore size distributions of samples: (a) cumulative curves of samples with 0% bentonite, (b) density function curves of samples with 0% bentonite, (c) cumulative curves of samples with 10% bentonite, (d) density function curves of samples with 10% bentonite, (e) cumulative curves of samples with 20% bentonite, (f) density function curves of samples with 20% bentonite, (g) cumulative curves of samples with 30% bentonite, (h) density function curves of samples with 30% bentonite, (i) cumulative curves of samples with 50% bentonite, (j) density function curves of samples with 50% bentonite, (k) cumulative curves of samples with 70% bentonite and (l) density function curves of samples with 70% bentonite

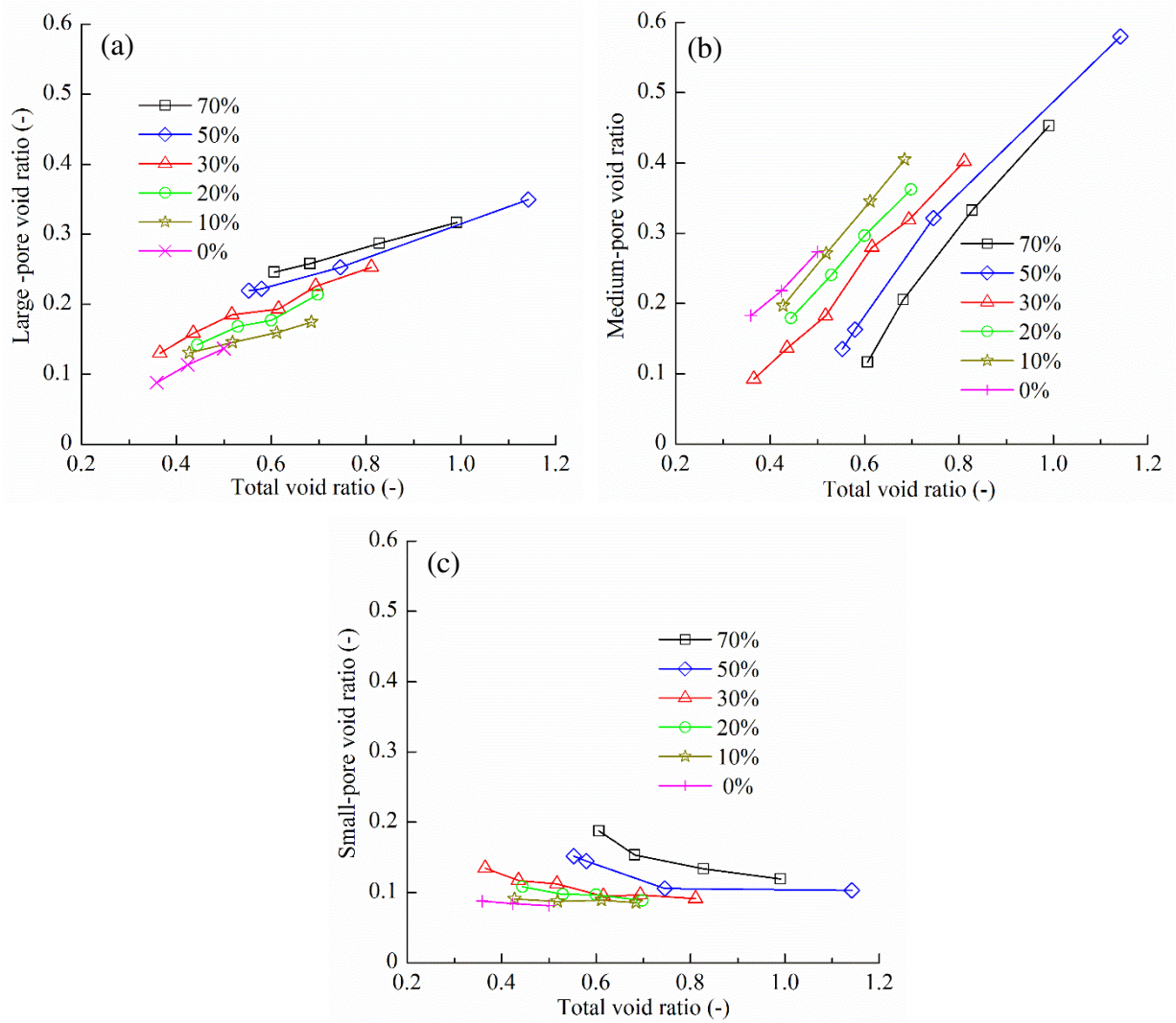


Fig. 7 Variations of (a) large-pore, (b) medium-pore and (c) small-pore void ratios with respect to total void ratio

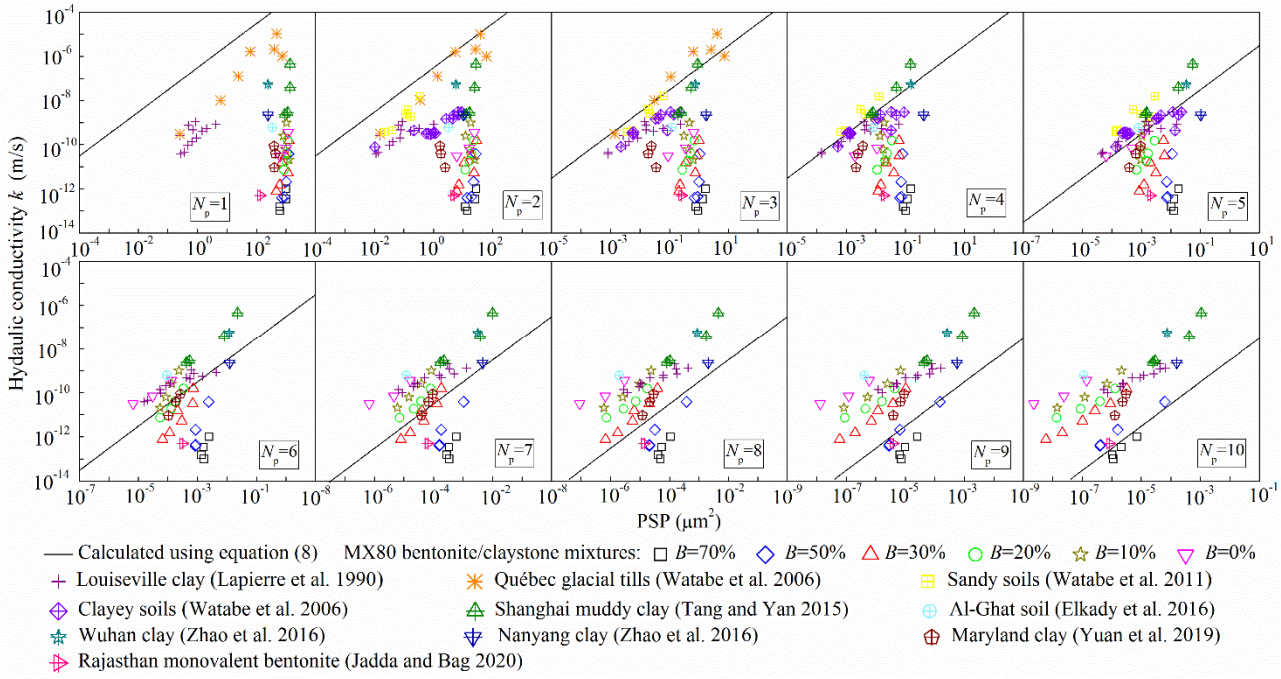
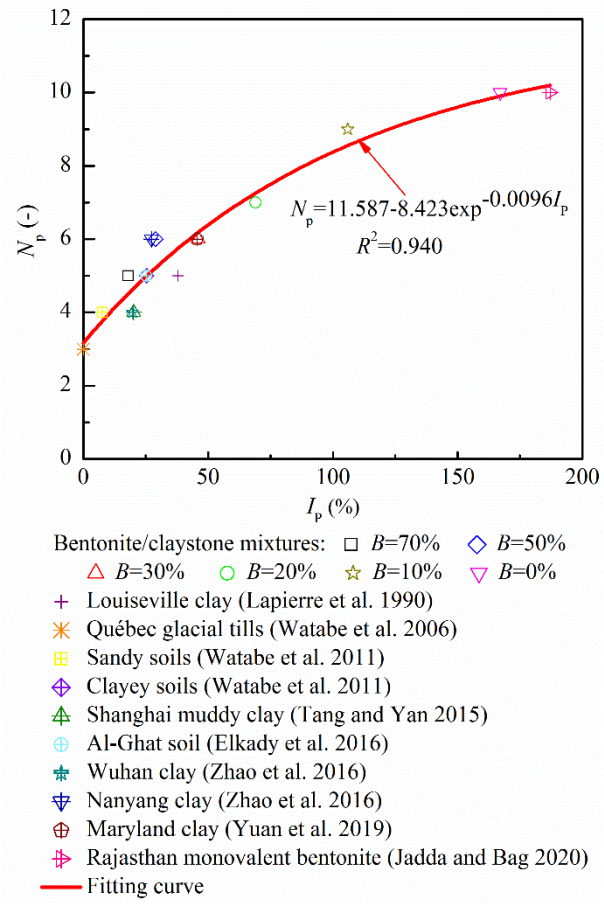


Fig. 8 Relationship between hydraulic conductivity and PSP



528
529

Fig. 9 Variation of N_p with plasticity index I_p

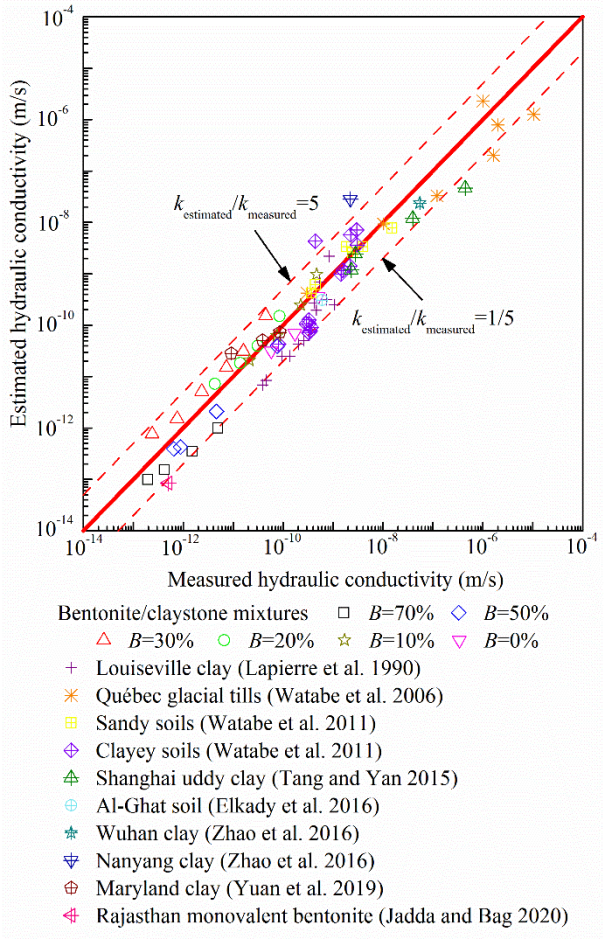


Fig. 10 Comparison between measured and estimated hydraulic conductivities using Eqs. (8), (10) and (11)

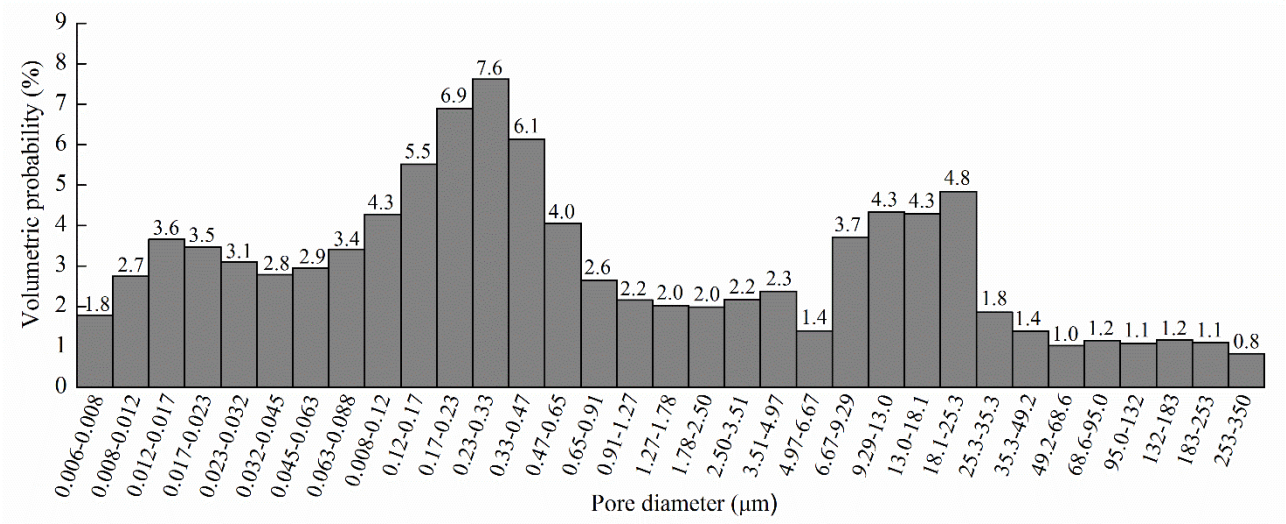


Fig. A1 Pore volumetric probability versus pore diameter for the sample with a bentonite fraction of 30% and void ratio of 0.62. The number above each bar indicates the pore volumetric probability in percent

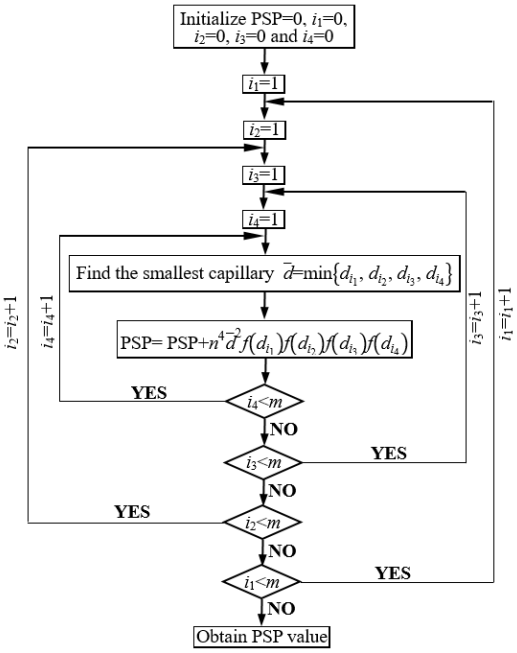


Fig. A2 The flowchart of calculating the PSP value using Eq. (10) with N_p=4